# Selective Catalytic Reduction of CO2 to CO by a Single-Site Heterobimetallic Iron–Potassium Complex Supported on Alumina

Abdulrahman Adamu Isah, Oluwatosin Ohiro, Li Li, Yahaya Nasiru, Kai Szeto, Pierre-Yves Dugas, Anass Benayad, Aimery De mallmann, Susannah Scott, Bryan Goldsmith, et al.

# Selective Catalytic Reduction of $CO_2$ to CO by a Single-Site Heterobimetallic Iron-Potassium Complex Supported on Alumina

Abdulrahman Adamu Isah,[a,e] Oluwatosin Ohiro,[b] Li Li,[c] Yahaya Nasiru,[a] Kai C. Szeto,[a] Pierre-Yves Dugas,[a] Anass Benayad,[d] Aimery De Mallmann,[a] Susannah L. Scott,[c]* Bryan R. Goldsmith,[b]* and Mostafa Taoufik[a]*

[a]*Université Lyon 1, Institut de Chimie Lyon, CPE Lyon CNRS, UMR 5128, CP2M, CPM, 43 Bd du 11 Novembre 1918, 69616 Villeurbanne Cedex, France.*

[b]*Department of Chemical Engineering, University of Michigan Ann Arbor, MI 48106, USA*

[c]*Department of Chemical Engineering, and Department of Chemistry & Biochemistry, University of California, Santa Barbara, California 93106, USA*

[d]*Université Grenoble Alpes, CEA−LITEN, 17 rue des Martyrs, 38054 Grenoble Cedex 9, France.*

[e]*Department of Pure and Environmental Chemistry, Usmanu Danfodiyo University, Sokoto, Nigeria*

**Keywords**: surface organometallic chemistry, heterobimetallic complexes, XAFS, reverse water gas shift reaction

**Abstract**

$CO_2$ has attracted much attention as a $C_1$-feedstock for synthetic fuels via its selective catalytic hydrogenation to liquid hydrocarbons. One strategy is the catalytic reduction of $CO_2$ to CO through the reverse water-gas shift (RWGS) reaction, followed by the hydrogenation of CO. In this work, potassium *tris*(tert-butoxy)ferrate, $[\{(THF)_2KFe(O\textit{t}Bu)_3\}_2]$, was supported on alumina that had been partially dehydroxylated at 500 °C ($Al_2O_{3\text{-}500}$) and the resulting catalyst was investigated in the selective reduction of $CO_2$ to CO. The active site precursor was identified as $[(THF)K(Al_sO)Fe(O\textit{t}Bu)_2(OHAl)]$ (i.e., $[(THF)KFe(O\textit{t}Bu)_2]/Al_2O_{3\text{-}500}$), denoted **2-K**, based on elemental analysis, DRIFT spectroscopy, scanning electron microscopy with energy-dispersive X-ray spectroscopy (HRTEM and EDS), X-ray photoelectron spectroscopy, and X-ray absorption spectroscopy. Under reaction conditions, the precursor becomes an active, stable, and selective RWGS catalyst (100% selectivity to CO at 22.5% $CO_2$ conversion). The reaction mechanism was studied by *operando* DRIFT spectroscopy and density functional theory (DFT) modeling. The results are consistent with a mechanism involving $H_2$ activation by $K[(Al_sO)_2FeOH]$, leading to $K[(Al_sO)_2FeH]$. $CO_2$ insertion gives a hydroxycarbonyl intermediate $K[(Al_sO)_2FeCOOH]$, followed by liberation of CO to regenerate $K[(Al_sO)_2FeOH]$.

## Introduction

The dramatic increase in atmospheric $CO_2$ concentration over the last several decades is contributing to harmful environmental changes such as global warming and ocean acidification. Technologies that reduce $CO_2$ emissions are actively being sought. Recent research has advanced the prospects for carbon capture and storage, as well as carbon capture and utilization (CCU).[1,2] Multiple studies suggest that CCU has the potential to be the more valuable and sustainable approach.[3,4] In CCU, $CO_2$ serves as a $C_1$ feedstock to manufacture fuels and chemicals.[5,6] However, activation of $CO_2$ and its selective conversion to desired products requires an appropriate catalyst and a source of energy.[7–11] Thermocatalytic processes that use $CO_2$ have fairly simple reactor designs and can, in principle, be operated at commercial scales to produce a range of carbon-based products, including CO, formaldehyde, methanol, methane, or light olefins (e.g., ethylene, propylene),[12,13] depending on the catalyst. These energy-intensive processes must be highly selective in order to be cost-effective.

The reverse water-gas shift (RWGS) reaction [Eq. 1] converts $CO_2$ to CO, an important intermediate in the production of higher-value chemicals and fuels via Fischer-Tropsch and methanol syntheses. RWGS is already used in many existing industrial processes. However, competing $CO_2$ methanation [Eq. 2] and methanol formation lower the CO selectivity.[5,6,14–16] The methanol yield is often negligible in atmospheric pressure reactions,[17] but $CO_2$ methanation is highly exothermic and is thermodynamically favored over the endothermic RWGS at moderate reaction temperatures.[17–19]

$$CO_2 + H_2 \rightleftarrows CO + H_2O_{(g)} \qquad \Delta H^e = 41.3 \text{ kJ/mol} \qquad (1)$$

$$CO_2 + 4\ H_2 \rightleftarrows CH_4 + 2\ H_2O_{(g)} \qquad \Delta H^e = -164.7 \text{ kJ/mol} \qquad (2)$$

A current challenge is the development of catalysts capable of producing CO selectively at these moderate temperatures. Furthermore, because CO is an intermediate in the production of other hydrocarbons from $CO_2$, understanding the RWGS mechanism will advance the design of catalysts for these more complex processes.[20]

RWGS catalysts generally possess two functionalities, both typically involving transition metal sites: (1) the ability to bind $CO_2$ and activate one C=O bond to generate adsorbed oxygen, and (2) the ability to dissociate $H_2$, resulting in the hydrogenation of adsorbed oxygen to form water. A selective RWGS catalyst will not dissociate CO, preventing its hydrogenation.[21] Selective RWGS catalysts that are highly active require judiciously chosen active phases. Noble metals such as Pt and Pd are good $H_2$ activation catalysts, but they are less effective at binding and activating $CO_2$, which typically requires a mildly oxophilic metal such as Ru or Rh.[22–24] The activity and selectivity of the transition metal can be altered by support effects, the nature of the active phase, and the presence of promoters (e.g., alkali metals, reducible transition metal oxides).

Nanoparticles of Ni, Rh, and Ru tend to catalyze $CO_2$ methanation rather than form CO selectively.[25–28] However, the metal ensemble size affects the outcome of $CO_2$ hydrogenation; $CH_4$ is the major product when the catalyst consists mainly of metal nanoparticles, whereas CO is typically the major product when the metal sites are atomically dispersed.[25,27] For example, the selectivity of a Ru single-atom catalyst towards CO decreased with time on-stream at 350 °C, gradually shifting towards methane as Ru nanoparticles were formed by sintering of the active single sites.[25] In that case, a strong metal-support interaction was important to ensure catalyst stability and avoid the undesired formation of nanoparticles.

The presence of alkali metal ions can enhance metal-support interactions for transition metal-based catalysts, leading to increased stability and thereby increased CO selectivity.[29,30] For example, the addition of $Li^+$ to a Rh-exchanged Y-zeolite catalyst greatly improved its RWGS

activity and produced mainly CO, in contrast to unpromoted Rh-Y which was more selective for methane.[31] $Li^+$ was suggested to enhance $CO_2$ adsorption and promote its reaction with $H_2$ to form oxygenates such as formates or carboxylates, which can decompose to CO and $H_2O$.[20,32] Similarly, $K^+$-promotion of a conventional $Fe/Al_2O_3$ catalyst (K/Fe = 1) resulted in a tripling of the CO formation rate.[33] However, the active site of this catalyst and its reaction mechanism are unclear: based on gas-switching experiments, both redox and associative mechanisms were suggested to occur. The FeK/γ-$Al_2O_3$ catalyst also deactivated linearly with time on-stream, probably due to a loss of oxidized iron species (evident in the XANES), leading to sintering and the formation of FeK clusters. A similar observation was reported for supported $Ru/Al_2O_3$ catalysts at low Ru loading. Monitoring the evolution of this catalyst via STEM imaging during a temperature programmed reaction showed that Ru single atoms sinter into 3D clusters, causing a drop in CO selectivity concurrent with the formation of methane.[25] Another study suggested that $K^+$ increases the basicity of the catalyst, enhancing the adsorption and activation of $CO_2$.[34,35] The mechanism was proposed to involve CO formation by decomposition of a formate intermediate.

Design principles for a selective RWGS catalyst can be formulated using these ideas. The aim is to achieve a stable, high dispersion of moderately oxophilic transition metal ions on an oxide support, in proximity to alkali metal cation promoters. Environmental and economic considerations dictate that the active phase should be a non-toxic and, preferably, non-precious metal. Fe is a promising candidate because Fe compounds are known to reduce $CO_2$ to give CO, formic acid/formate, methanol, and/or methane.[36] However, reports of Fe as a RWGS catalyst selective towards CO are rare. Generally, Fe-based catalysts are known to be effective in $CO_2$ methanation, particularly when the catalyst contains Fe clusters or nanoparticles.[37] Studies of isolated Fe species as active sites for $CO_2$ reduction are limited, and a detailed reaction mechanism has yet to be proposed.

A CO-selective RWGS catalyst can be achieved by using surface organometallic chemistry to create a well-defined, supported single-site Fe catalyst. This catalyst has a low loading to avoid the formation of FeK nanoparticles and consequently deactivation and loss of selectivity to CO. Compared to single atom catalysis comprising a naked isolated metal site on the support, surface organometallic chemistry could lead to a more predictive catalytic system in heterogeneous catalysis with the possibility to control by judicious chose of the ligand environment of the metal, giving the desired active species.[38]

Alumina (AEROXIDE ALUC alumina from Evonik, 105 $m^2.g^{-1}$) was chosen as the support to stabilize the isolated Fe species, and alkali metal cations were incorporated as promotors. Molecular heterobimetallic complexes containing the complex monoanions $[Fe(O\textit{t}Bu)_3]^-$ or $[Fe(ditox)_3]^-$ (ditox = $\textit{t}Bu_2(Me)C\text{-}O$) with $M^+$ (M = Na, K, Li) as the counter-cation have the desired stoichiometry and (potentially) proximity between Fe and alkali metal ion to promote the reaction. The O*t*Bu or ditox ligands were chosen because recent work has shown that moderate thermal treatment can lead to well-defined metal-oxo/oxide surface species by β-H elimination and release of disubstituted α-olefins.[39]

In this work, the dimeric molecular complexes $[\{(THF)_2KFe(O\textit{t}Bu)_3\}_2]$ and $[\{(THF)NaFe(O\textit{t}Bu)_3\}_2]$ and the monomeric molecular complex $[(THF)LiFe(ditox)_3]$ were supported on an alumina that had been partially dehydroxylated at 500 °C ($Al_2O_{3\text{-}500}$), to obtain supported mononuclear complexes $[(Al_sO)Fe(O\textit{t}Bu)_2]^-M^+$ (M = Na and K) or $[(Al_sO)Fe(ditox)_2]^-Li^+$ (where $Al_s$ designates a surface Al site). The materials were characterized using ICP, DRIFTS, HRTEM, EDX, XPS, EPR, and XAFS. The supported Fe complexes were activated by thermolysis in flowing Ar in a packed-bed reactor, then used directly to catalyze the reduction of $CO_2$ to CO, with particular interest in the effect of the alkali metal promoter. Density functional theory (DFT)

and mean-field microkinetic modeling were performed to shed light on the RWGS mechanism by the best-performing $K^+$-promoted Fe-complex catalyst.

## Experimental methods

### Chemicals and materials

All experiments were carried out under a controlled atmosphere, using Schlenk and glovebox techniques for organometallic synthesis. For the synthesis and treatment of supported species, reactions were carried out using high-vacuum lines (*ca.* $10^{-5}$ mbar) and gloveboxes. Pentane and THF were distilled from NaK and degassed using freeze-pump-thaw cycles. $FeBr_2$ and *t*BuOK were purchased from Aldrich and used as received. All characterization was performed under an inert atmosphere, except for EDX/STEM/HRTEM for which sample preparation was carried out in air. Catalytic tests were performed in a ½'' stainless-steel continuous flow reactor connected to an online GC (Agilent Technologies 7890A) equipped with a FID (Jetanyzer$^{TM}$). The products were separated on a 30-m PLOT Q and CarbonPlot columns connected in series. Elemental analysis was carried out at the Mikroanalytiches Labor Pascher, Ramgen, Germany, and CREALINS, Villeurbanne, France, using an iCAP 6500 Duo inductively-coupled plasma atomic emission spectrometer (Thermo Scientific). All samples sent for elemental analysis were prepared under Ar and sealed under high vacuum ($10^{-5}$ mbar).

Infrared spectra were recorded in diffuse reflectance mode on a Nicolet 6700 FT-IR spectrometer, in an air-tight cell with $CaF_2$ windows under an atmosphere of Ar at room temperature. For X-ray Photoelectron Spectroscopy (XPS), samples were sent in sealed vials to CEA-Liten, Grenoble, where survey spectra (1.6 eV resolution) and high-resolution spectra (0.6 eV resolution) were recorded. For X-ray absorption spectroscopy, samples were sent in sealed vials to the Stanford Synchrotron Radiation Lightsource (SSRL). High Resolution transmission electron microcopy (TEM) and Energy Dispersive X-ray (EDX) spectroscopy were performed at

the Centre Technologique des Microsructures, Université Lyon 1. Prior to EDX/STEM/HRTEM analysis (JEOL 2100F, 200 kV), samples were prepared by placing a spot of a suspension containing the test material on an ultrathin Ni grid. Single crystal X-ray diffraction (XRD) was recorded at the Institut des Sciences Analytiques Lyon 1.

Electron paramagnetic resonance (EPR) spectroscopy was carried out with a Bruker spectrometer Elexsys E500 using X Band (9.4 GHz) radiation at T = 110–120 K, in the Laboratoire de Chimie, ENS Lyon. Samples for EPR were prepared in air-tight quartz tubes loaded inside a glove box. For quantitative studies of the paramagnetic phase, double integration of the EPR signal was performed and compared to that of a reference composed of a known amount of vanadyl(IV) sulfate. A Micromeritics ASAP 2020 (surface area and porosity analyzer) was used for the determination of textural properties (e.g., Brunauer-Emmett-Teller, B.E.T. surface area). Off-line gas chromatographic analyses were performed on an HP 5890 series II GC, equipped with an HP5 GC column and FID detector.

**Catalyst preparation**

*Synthesis of molecular iron complexes.* $[\{(THF)_2KFe(O\textit{t}Bu)_3\}_2]$ was synthesized by adapting a method used for the preparation of $[\{(THF)NaFe(O\textit{t}Bu)_3\}_2]$.[40] A solution of *t*BuOK (1.56 g; 13.9 mmol) in THF (40 mL) was transferred by cannula into a solution of $FeBr_2$ (1 g; 4.6 mmol) in THF (40 mL) under vigorous stirring (600–800 rpm) at room temperature. The resulting green solution was stirred for 12 h. The solution was filtered by cannula and the solvent was evaporated at room temperature under reduced pressure. The resulting residue was extracted with dry n-hexane (10 ml) and the solution was filtered through a pad of Celite. The filtrate was concentrated under dynamic vacuum ($10^{-2}$ mbar) to one-fourth its original volume, then cooled at –24 °C overnight for crystallization. The remaining hexane was removed by cannula filtration and the resulting solid was dried under vacuum ($10^{-2}$ mbar) to obtain a pale-yellow powder (62 % yield). Elemental

analysis (ICP-AES): calculated (%) for $K_2Fe_2C_{40}H_{86}O_{10}$: K, 8.53; Fe, 12.18; C, 52.40; H, 9.39. Found (%): K, 8.55; Fe, 12.11; C, 52.36; H, 9.44. [{(THF)NaFe(O*t*Bu)$_3$}$_2$] and [{(THF)LiFe(ditox)$_3$}$_2$] (ditox = *t*Bu$_2$MeCO) were synthesized according to literature procedures.[40,41]

*Pretreatment of $Al_2O_{3-500}$ support.* A literature procedure was adopted to prepare $Al_2O_{3-500}$.[42] A slurry of fumed aluminum oxide (20 g; Evonik, B.E.T. surface area 105 $m^2\ g^{-1}$, density 0.55 g $mL^{-1}$, 1.8 OH/$nm^2$ (0.28 mmol/g) in distilled water was placed in an oven (120 °C) for 24 h to compact it. The sample was ground and sieved (400 mesh). The powder was then calcined at 500 °C for 16 h in a flow of dry air (50 mL/min). The sample was partially dehydroxylated at 500 °C under high vacuum ($10^{-5}$ mbar) for 24 h to produce $Al_2O_{3-500}$.

*Grafting of molecular complexes onto $Al_2O_{3-500}$.* A solution of [{(THF)$_2$KFe(O*t*Bu)$_3$}$_2$] (0.25 g) solution in n-pentane (15 mL) was added to 3 g $Al_2O_{3-500}$ to produce a solid containing *ca.* 1 wt% Fe. The brownish suspension was stirred for 24 h at room temperature, then filtered through a glass frit. The solid was dried under high vacuum ($10^{-5}$ mbar) while the filtrate was analyzed by GC. The same procedure was used to graft [{(THF)NaFe(O*t*Bu)$_3$}$_2$] and [{(THF)LiFe(ditox)$_3$}$_2$] onto $Al_2O_{3-500}$ (all *ca.* 1 wt% Fe).

*Catalytic testing.* Catalysts were evaluated in a continuous flow stainless steel reactor equipped with a 4-way valve and coupled to an online GC. The reactor was charged with catalyst (250 mg) in the glovebox and the gas lines were purged with the reactant gas before exposing the catalyst to them. The gas flow was controlled using Bronkhorst mass flow controllers. The GC is equipped with two columns in series: a carbon Plot column to separate $CO_2$, CO, and $CH_4$, and a Plot Q column to separate higher hydrocarbons. The gas effluent from the reactor passes through both columns before reaching the detectors. The separated products were detected by TCD and FID (equipped with a Jetanizer methanizer), connected in series.

Catalytic tests were performed using a certified gas mixture with a $H_2/CO_2$ ratio of 3 (Mélange Crystal, Air Liquide), at a constant flow rate of 3 mL $min^{-1}$ (measured at room temperature). Prior to starting the reaction, the catalyst was activated in situ in a flow of Ar for 2 h at 300 °C. $CO_2$ conversion and product molar selectivities were calculated according to Eqs. 3–5.

$$Conversion\ (CO_2) = \frac{(CO_2)inlet - (CO_2)outlet}{(CO_2)inlet} \times 100\% \quad (3)$$

$$Selectivity\ to\ CO = \frac{(CO)outlet}{(CO_2)inlet - (CO_2)outlet} \times 100\% \quad (4)$$

$$Selectivity\ to\ CH_4 = \frac{(CH_4)outlet}{(CO_2)inlet - (CO_2)outlet} \times 100\% \quad (5)$$

**Computational methods**

The mechanism of the RWGS reaction was investigated using Kohn-Sham density functional theory (DFT) as implemented in Vienna Ab initio Simulation Package (VASP) software.[43–45] The revised Perdew-Burke-Ernzerhof (RPBE) functional was selected because it is more accurate for predicting adsorption energies of molecules such as CO on surfaces compared to PBE. The Grimme D3 correction was included to treat long-range dispersion.[46] The projector augmented wave method was used. The kinetic energy cutoff for plane wave calculations was 400 eV. A Γ-centered 3×3×1 Monkhorst-Pack k-point mesh was used to sample the Brillouin zone for surface reaction calculations.

The lattice constants for bulk γ-$Al_2O_3$ (i.e., 5.512, 8.306, and 7.996 Å) computed using the RPBE functional are similar to those computed previously (5.587 Å, 8.413 Å, 8.068 Å).[45] The unit cell of γ-$Al_2O_3$ was expanded to form a five-layered 2×2×1 γ-$Al_2O_3$ slab with the (110) surface facet exposed. Periodic boundary conditions were imposed in all three spatial dimensions with a vacuum layer of 15 Å in the z-direction to ensure no interaction between periodic images. The

bottom three layers of the γ-$Al_2O_3$(110) slab were fixed to mimic the bulk, while the top two surface layers were allowed to relax. The (110) facet was chosen because of its abundance on γ-$Al_2O_3$.[47–49]

All calculations involving Fe were spin-polarized. Electronic optimization process continued until the energy difference between consecutive electronic steps was less than $10^{-4}$ eV, and geometry optimization of the ionic structure was carried out until the maximum ionic force dropped below 0.05 eV/Å. Transition states were calculated using the climbing image nudged elastic band (NEB) algorithm and the dimer method. Seven intermediate images between the initial and final states were pre-converged with NEB to estimate the reaction pathway, and then the dimer method was used to find the first-order saddle point of the highest image until the forces converged to a maximum of 0.05 eV/Å. Ideal gas statistical mechanics were used to obtain Gibbs' energies from the DFT-calculated 0 K electronic energies for reaction mechanism modeling. Detailed procedures for all the thermodynamic corrections and mean-field microkinetic modeling are given in the Supporting Information (SI).

**Results and discussion**

**Synthesis and characterization of a heterobimetallic iron complex**

Although heterobimetallic [{$(THF)_2KFe(OtBu)_3$}$_2$], **1**, has not previously been reported, its synthesis was achieved by adapting a method used for the preparation of the sodium analog, [{$(THF)NaFe(OtBu)_3$}$_2$].[40] Complex **1** was crystallized from a concentrated THF solution at –25 °C. Single crystal X-ray diffraction confirmed that **1** is dimeric, with an Fe-Fe distance of 3.2905 Å (**Figure 1**). The structure can be described as a dinuclear assembly of two units, each composed of one Fe atom, one K atom, three O*t*Bu ligands, and two THF molecules, in the monoclinic $P2_1/n$ space group. The core consists of a $K_2O_6Fe_2$ cage with $C_2$ symmetry, similar to the fragment present in the $Na^+$-containing heterobimetallic analog.[40] In complex **1**, each Fe atom is coordinated

by two $\mu^2$- and two $\mu^3$-O*t*Bu bridging ligands, with O-Fe-O angles ranging from 75.086 to 139.137 °. The Fe atoms have distorted tetrahedral coordination. As expected, the $Fe_2O(\mu^3)$ bond lengths [2.0708 and 2.0791 Å] are longer than the $Fe_2O(\mu^2)$ bond lengths [1.9132 and 1.9179 Å]. The $K^+$ is coordinated by the oxygen atoms of one $\mu^3$-O*t*Bu and two $\mu^2$-ligands, as well as two THF molecules (at 2.695 and 2.728 Å), in a distorted trigonal bipyramidal arrangement. The O(1)-K-O(2) and O(2)-K-O(3) angles vary between 68.75 and 171.04 °. The two K-O distances in the K-($\mu^2$-O*t*Bu) fragment are 2.5852 Å and 2.6186 Å. As expected, the K-O distance in the K($\mu^3$-O*t*Bu) fragment (2.9054 Å) is longer than in the K($\mu^2$-O*t*Bu) fragment.

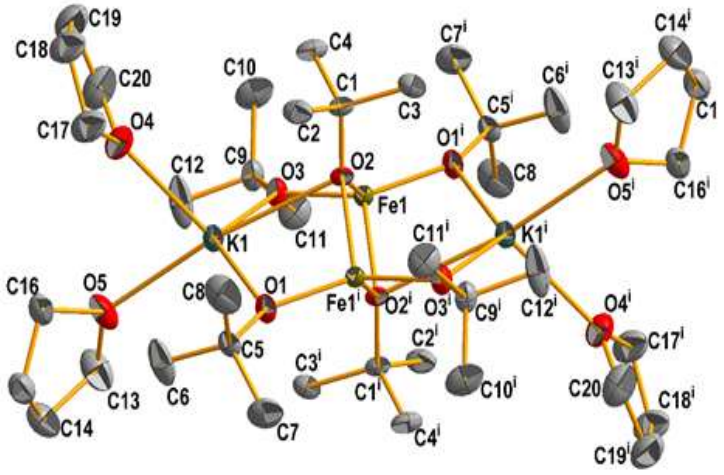


**Figure 1.** X-ray crystal structure of [{(THF)$_2$KFe(O*t*Bu)$_3$}$_2$], **1**, with thermal ellipsoids plotted at the 30% probability level. H atoms have been removed for clarity. Selected bond lengths (Å) and angles (°): Fe(1)-O(1) 1.9132(15), Fe(1)-O(2) 2.0708(14), Fe(1)-O(3) 1.9179(15), Fe(1)-O(2a) 2.0791(14), Fe(1)-K(1) 3.3607(6), Fe(1)-K(1a) 3.3697(6), K(1)-O(3) 2.5852(15), K(1)-O(1a) 2.6186(16), K(1)-O(2) 2.9054(8), K(1)-O(4) 2.695(2), K(1)-O(5) 2.728(2) Å; O(1)-Fe(1)-O(2) 109.05(6), O(1)-Fe(1)-O(3) 139.14(6), O(2)-Fe(1)-O(3) 109.05(40), O(1)-Fe(1)-O(2a) 103.39(6), O(1a)-K(1)-O(2) 68.92(4), O(1a)-K(1)-O(3) 125.56(5), O(2)-K(1)-O(3) 68.75(11)°.

Elemental analysis of complex **1** (ICP-AES for Fe and K, and combustion analysis for C) is consistent with the molecular formula [{(THF)$_2$KFe(O*t*Bu)$_3$}$_2$], with atomic ratios of Fe/K = 1.01 (theor. 1), C/Fe = 20.1 (theor. 20) and H/Fe = 43.2 (theor. 43). The DRIFT spectrum contains ν(C-

H) bands at 3000–2900 $cm^{-1}$, as well as multiple peaks in the range 1500–1200 $cm^{-1}$, assigned to $\delta(CH_x)$ modes of THF and tBuO (**Figure S1**). Only traces of Fe(III) (less than 3 mol%, **Figure S2**) were observed by EPR.

**Synthesis and characterization of the supported $K^+$-containing iron complex**

The reaction of an *n*-pentane solution of **1** with alumina that had been partially dehydroxylated at 500 °C ($Al_2O_{3\text{-}500}$) was allowed to proceed at room temperature for 12 h to produce a solid containing the supported Fe complex, hereafter denoted **2-K**. This material was washed with fresh pentane and dried under vacuum, affording a pale-yellow material. THF and *t*BuOH formed during the grafting step were identified by GC analysis. The DRIFT spectrum reveals that the surface OH groups of alumina (ν(O-H); 3795–3660 $cm^{-1}$) were partially consumed by the grafting reaction (**Figure 2**). Less reactive OH groups remain, as has been observed in the grafting of other metal complexes.[50] Simultaneously, bands corresponding to the organic ligands appeared at 3000–2800 $cm^{-1}$ (ν(C-H)); 1466 and 1455 $cm^{-1}$ ($\delta(CH_x)$) and at 1380 and 1356 $cm^{-1}$ ($\delta(CH_3)$).

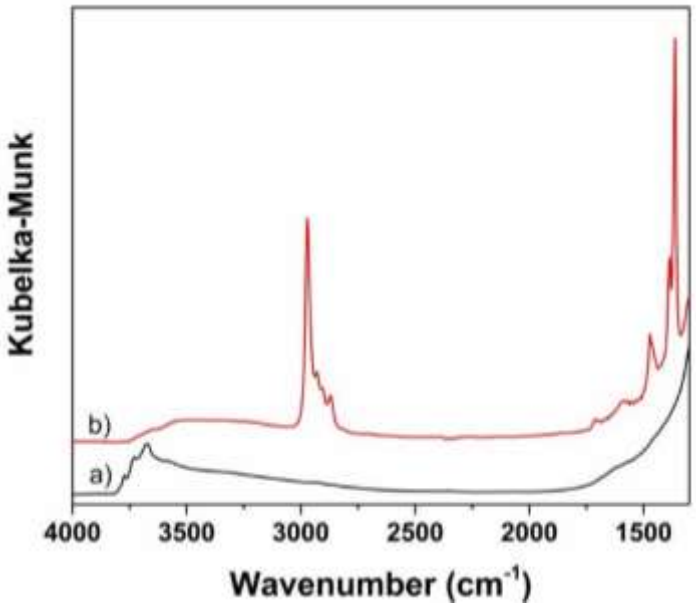


**Figure 2**. DRIFT spectra of **(a)** unmodified $Al_2O_{3\text{-}500}$ (black), and **(b)** after reaction of $[\{(THF)_2KFe(OtBu)_3\}_2]$ **1** with $Al_2O_{3\text{-}500}$ to give **2-K** (red).

ICP-AES analysis confirmed the presence of Fe (1.1 wt%), K (0.98 wt%), and C (2.86 wt%) in the grafted material, which corresponds to a ratio Fe/OH = 0.70. The C/Fe atomic ratio of 11 is consistent with the loss of one O*t*Bu ligand and one THF per Fe (expected C/Fe = 12). The Fe/K atomic ratio of 1.1 shows that the solid retains essentially all the original $K^+$ in the grafted complex. The Fe/K ratio of 1 is also supported by EDX analysis, which further indicates that Fe and $K^+$ are well dispersed on the surface (**Figures S3** and **S4**). No agglomeration of Fe or $K^+$ is observed by HRTEM (**Figure S5**). EPR spectroscopy of **2-K** shows evidence for only a small amount of Fe(III) (< 3%, **Figure S6**). This small amount is probably due to traces of Fe(III) in the molecular complex **1**.

The alumina-supported Fe complex **2-K** is therefore formulated as [(THF)K($Al_s$O)Fe(O*t*Bu)$_2$]), where $Al_s$ represents a surface aluminum. It was further investigated by XPS. Quantitative analysis of the XPS survey scan[51] confirms that the Fe 2$p_{3/2}$ and K 2*s* signals reflect an Fe:K atomic ratio of 1.0. A representative high-resolution spectrum in the Fe 2*p* region shows two signals corresponding to the expected spin-orbit doublet (**Figure S7**), with the intensity of the Fe 2$p_{3/2}$ signal being twice that of the Fe 2$p_{1/2}$ signal, as expected. The Fe 2$p_{3/2}$ signal is broad (FWHM 4.3 eV) and centered at 710.4 eV. This chemical shift is intermediate between values reported for $Fe_2O_3$ and FeO.[52,53] Although oxidation states for iron oxides and iron metal may be inferred from the Fe 2$p_{3/2}$ chemical shift, interpretation of the XPS for molecular Fe complexes is complicated by geometry and spin state.[54] However, the oxidation state in **2-K** is predominantly Fe(II), based on the EPR analysis (**Figure S6**).

The structure of **2-K** was studied by X-ray absorption fine structure (XAFS) spectroscopy at the Fe K-edge. The XANES of **1** and **2-K** are similar, especially in the region below 7125 eV (**Figure S8**), suggesting that the Fe(II) sites in the supported complex are also non-octahedral, e.g., in distorted tetrahedral or trigonal coordination. The EXAFS curve fit for **2-K** is shown in **Figure 3**, with parameters in **Table 1**. The results are consistent with the iron having a first coordination

sphere similar to that of Fe in the monomeric heterobimetallic complex $[(THF)_2KFe(ditox)_3]$ (ditox = $t$Bu$_2$(Me)CO$^-$).[40] The Fe center in **2-K** is proposed to have trigonal planar geometry, with one oxygen atom at 1.84 Å and two more at 2.20 Å. The shorter distance is in the range of Fe-OR bond lengths observed by XRD for terminal alkoxides,[40] whereas the longer distance more closely resembles that of the bridging alkoxides in dimeric **1** (average 2.075 Å, **Figure 1** and **Table 1**). The even longer distance in **2-K** may be due to steric constraints in the surface species, with oxygen atoms shared between iron centers and Lewis acidic surface Al sites.

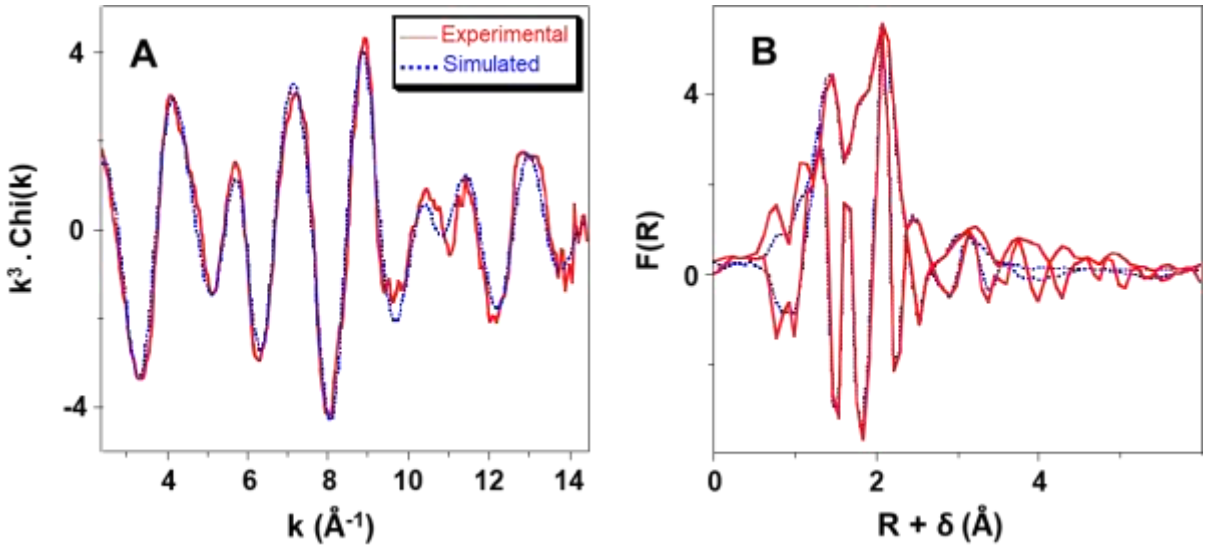


**Figure 3.** The $k^3$-weighted Fe K-edge EXAFS of **2-K**, in **A**: $k$-space, and **B**: R-space (FT modulus and imaginary part). Solid red lines: experimental data; dashed blue lines: curvefit obtained using spherical wave theory.

**Table 1.** Comparison of EXAFS curvefit parameters for **2-K**[a] with distances of molecular analogs[b, c]

| | EXAFS results | | | XRD values | |
|---|---|---|---|---|---|
| **Path** | ***N*** | ***R* (Å)** | **σ² (Å²)** | ***dimer d* (Å)[b]** | ***monomer d* (Å)[c]** |
| Fe-$O_1$(short) | 1.2(3) | 1.83(1) | 0.0021(8) | 1.915 ×2 | 1.826 ×1 |
| Fe-$O_2$(long) | 1.8(5) | 2.20(2) | 0.0068(17) | 2.075 ×2 | 1.903 ×2 |
| Fe--O(Al) | 2.5(4) | 2.63(2) | 0.0048(21) | | |
| Fe--C | 2.4(5) | 2.80(3) | 0.0089(35) | 3.079 | 3.053 |
| Fe--$Al_S$ | 1.1(3) | 3.10(4) | 0.0133(64) | | |
| Fe--K | 1.2(4) | 3.74(5) | 0.0133[d] | 3.361 | 3.357 |

[a] Errors generated by the EXAFS fitting program "RoundMidnight" are indicated in parentheses. Global fit parameters: $S_0^2 = 0.95$ and $\Delta E_0 = -(2.4 \pm 0.8)$ eV. $2.4 \le k \le 14.5$ Å$^{-1}$; $0.3 \le R \le 3.6$ Å. Fit residual $\rho = 4.9$ %; Quality factor $(\Delta\chi)^2/\nu = 2.85$ ($\nu = 10 / 28$). [b] Average distances from XRD structure of **1** (dimer). [c] Average distances from XRD structure of $Fe(ditox)_3K(THF)_2$ (monomer).[41] [d] Shell constrained to a parameter above.

A contribution from light atoms at 2.63 Å is attributed to *ca.* two oxygen atoms from the alumina surface. Similar parameters were obtained by fitting the $k^2$-weighted $\chi(k)$ data (1.1(3) O at 1.82(2) Å, $\sigma^2$ = 0.0027(15) Å$^2$; 1.9 O at 2.20(2) Å, $\sigma^2$ = 0.0082(36) Å$^2$; 2.4 O at 2.59(2) Å, $\sigma^2$ = 0.0039(23) Å$^2$). The fit was further improved by including additional shells of back-scatterers, in particular, *ca.* two C atoms at 2.80 Å, *ca.* one Al atom at 3.10 Å and *ca.* one K atom at 3.74 Å. Attempts to introduce of a supplementary level of Al scatters is not statistically validated. However, there is no evidence for a well-defined Fe-Fe path (expected at *ca.* 3.3 Å in a dimer structure), despite attempts to include it in the model. Based on this fit, the proposed monomeric structure for alumina-supported **2-K** is shown in **Scheme 1**, where the coordination spheres of iron and potassium are similar to those in **1**.

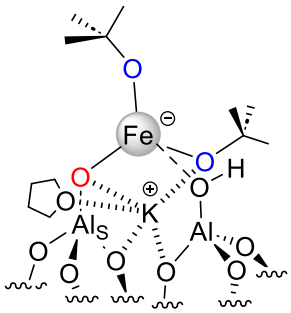


**Scheme 1.** Proposed monomeric structure for [(THF)K(Al$_s$O)Fe(O*t*Bu)$_2$(OHAl)] (i.e., **2-K**), prepared by grafting dimeric [{(THF)$_2$KFe(O*t*Bu)$_3$}$_2$], **1**, onto $Al_2O_{3\text{-}500}$. The structure is consistent with the XAFS analysis (the K coordination is proposed analogous to that of molecular complex **1**).

Overall, the evidence suggests that dimeric **1** dissociates during grafting and the monomer fragments react readily with alumina, affording isolated, bipodal [(THF)K(Al$_s$O)Fe(O*t*Bu)$_2$(OHAl)] species (**Scheme 1**). This species is proximal to a $K^+$ counter-cation, and with a labile proton that may be located on a coordinated oxygen from the alumina surface, or the O*t*Bu ligands, or may migrate between them. A preference for monomeric sites was previously observed in the grafting of [Al$^i$Bu$_3$]$_2$ (in equilibrium with its monomer in solution)[55] onto alumina, leading to a monomeric supported species.[56]

**Syntheses of other alkali metal-containing iron complexes and their supported analogs**

Dimeric [{(THF)NaFe(O*t*Bu)$_3$}$_2$] and monomeric [(THF)LiFe(ditox)$_3$] were prepared according to published procedures.[40,41] Each was grafted onto $Al_2O_{3\text{-}500}$, to obtain the complexes **3-Na** and **4-Li** (both *ca.* 1 wt% Fe), as described above, with the aim of comparing the effect of the alkali metal cation on the structure and catalytic activity of the supported iron complex. Complexes **3-Na** and **4-Li** were characterized by IR and ICP. The DRIFT spectrum of **3-Na** (**Figure S9**) is similar to that of **2-K** (**Figure 2b**). Elemental analysis revealed Fe, $Na^+$, and C contents of 0.90 (Fe/OH = 0.58), 0.37, and 2.18 wt%, respectively. The Na/Fe atomic ratio is 1.0, as expected, and the C/Fe atomic ratio, 11.3, is also consistent with the expected value (12). **4-Li** was assumed to react in a similar manner. Elemental analysis revealed Fe, C, and Li contents of 0.93 (Fe/OH = 0.60), 4.52, and 0.12 wt%, respectively. The Li/Fe atomic ratio, 1.0, is close to the expected value of 1. The C/Fe atomic ratio, 22.5, is close to the expected value of 24. The DRIFTS spectrum of **4-Li** (**Figure S10**) is also similar to **2-K** and **3-Na**.

Overall, these results suggest that dimeric [{(THF)$_2$KFe(O*t*Bu)$_3$}$_2$] and [{(THF)NaFe(O*t*Bu)$_3$}$_2$] undergo similar reactions with $Al_2O_{3\text{-}500}$, generating monomeric surface structures, exemplified by **2-K** in **Scheme 1**. Monomeric [(THF)LiFe(diox)$_3$] also seems to give a supported monomeric species.

**Catalytic activity in $CO_2$ hydrogenation**

The RWGS activity and CO selectivity of each catalyst (**2-K**, **3-Na**, and **4-Li**) were evaluated in a continuous flow reactor at 30 bar and 400 °C. **Table 2** compares the results for the three catalysts after 18 h on-stream. Clearly, the identity of the alkali metal promotor strongly alters RWGS activity and selectivity. The $K^+$-promoted Fe catalyst exhibits the highest $CO_2$ conversion (22.5%, well below the equilibrium value of *ca.* 45% to ensure meaningful kinetic measurements) and selectivity towards CO (100%). No significant deactivation of **2-K** was observed over the course

of 41 h (**Figure 4**). The high stability of **2-K** is likely due to the presence of well-dispersed isolated single sites, compared to a reported catalyst with a higher Fe loading that evolves to a material with a mixture of single sites and nanoparticles.[33] The presence of $K^+$ in proximity to Fe appears to stabilize Fe(II), and to provide a favorable site for $CO_2$ adsorption.

**Table 2**. Conversion and CO selectivity in $CO_2$ hydrogenation catalyzed by **2-K**, **3-Na**, or **4-Li**, after 18 h on stream.

| Catalyst | Conversion (%) | Selectivity (%) | |
|---|---|---|---|
| | | CO | $CH_4$ |
| **2-K** | 22.5 | 100 | - |
| **3-Na** | 4.0 | 93 | 7 |
| **4-Li** | 4.5 | 90 | 4* |

Reaction conditions: $CO_2/H_2$ = 1/3, volumetric flow rate = 3 mL $min^{-1}$, 400 °C, 30 bar, 250 mg catalyst. Note that the equilibrium conversion of $CO_2$ is *ca.* 45% for these reaction conditions. *Minor amounts of ethylene (0.6%), ethane (2.1%), propylene (1.1%), and propane (2.2%) were also observed.

In contrast, both **3-Na** and **4-Li** gave much lower conversions (ca. 4 %), and produced a mixture of CO and methane. For **3-Na**, the conversion decreased slightly with time on-stream (**Figure S11**), although its selectivity was rather stable (**Figure S12**).

The most promising catalyst, **2-K**, was investigated further by varying the reaction conditions. Decreasing the total pressure resulted in lower conversion but the same 100% CO selectivity (**Figure S13**). Similar behavior was observed at lower temperatures (**Figure S14**). These findings, supported by HRTEM performed after catalyst testing (**Figure S15**), suggest that the active site in **2-K** is robust under a range of reaction conditions, without sintering or other types of deactivation. The conversion increases linearly with pressure (**Figure S14**) at 350 °C, for an overall reaction order (i.e., combined reaction order for $CO_2$ and $H_2$) of 2.0.

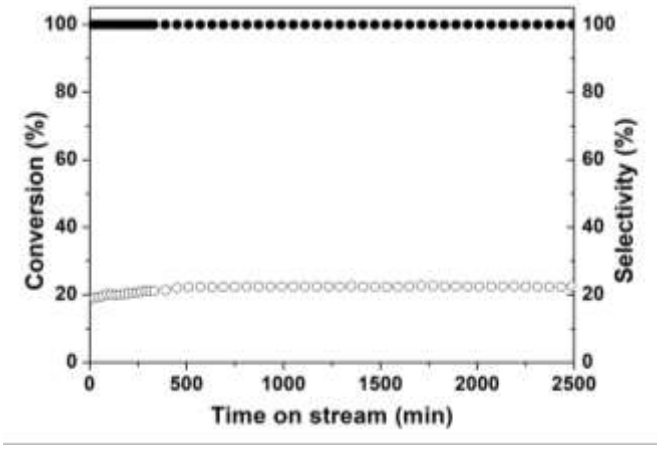


**Figure 4.** $CO_2$ conversion (open circles) and CO selectivity (filled circles) in the RWGS reaction catalyzed by **2-K**. Feed composition: $CO_2/H_2$ = 1/3, volumetric flow rate = 3 mL $min^{-1}$, 400 °C, 30 bar.

The thermal stability of **2-K** was evaluated by heating the catalyst in He while monitoring the catalyst with DRIFTS and the volatiles by GC–MS (**Figures S16 and S17**). The *t*BuO ligands are liberated as *t*BuOH from 50 to 250 °C, and as isobutene from 200 to 300 °C. We infer that **2-K** evolves at elevated temperatures to the iron hydroxyl complex shown as species **B** in **Scheme 2**. It is suggested to form by protonolysis of **1** by a residual hydroxyl group of the alumina surface to give species **A** with release of tBuOH (**Figure S16**), followed by decoordination of THF and β-H elimination liberating isobutene. Species **B** may add $H_2$ (according to DFT, by addition across an Fe-O bond, see below) leading to an iron hydride (Fe-H), species **C**, and release of water. Insertion of $CO_2$ gives the iron hydroxycarbonyl species **D**, followed by deinsertion and desorption of CO to regenerate the hydroxyl site **B**.

Insertion of $CO_2$ into an Fe-H bond leading to a formate has been reported.[57–60] However, previous reports[19,20] suggest that the major RWGS pathway involves a hydroxycarboxyl intermediate, while the formate pathway leads to oxygenates (e.g., formate and methanol). To explore these pathways, DFT calculations were carried out.

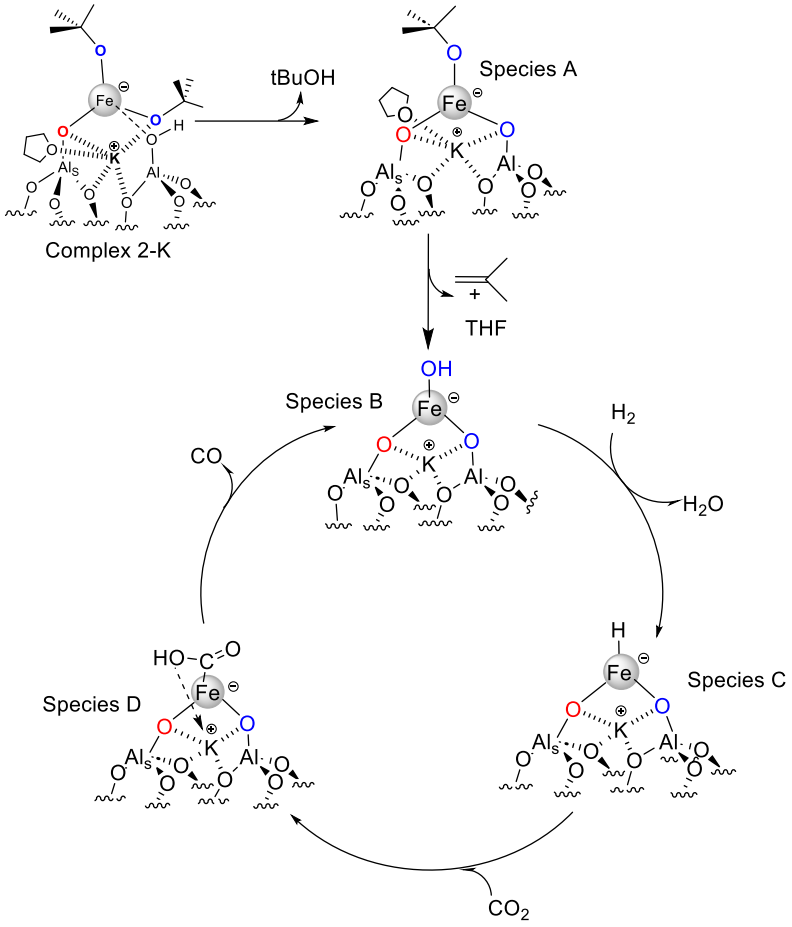


**Scheme 2.** Proposed mechanism for selective reduction of $CO_2$ to CO on catalyst **2-K**. Note that the reaction of **2-K** to give **A** requires a residual hydroxyl group from the alumina surface.

## Atomistic modeling of RWGS mechanism

The two postulated mechanisms for $CO_2$ hydrogenation catalyzed by **2-K** were probed using DFT modeling. First, a model of the grafted catalyst on alumina was constructed. Of the 31 unique sites probed for adsorbing Fe onto γ-$Al_2O_3$(110), the most stable location places the Fe between a tri-coordinated Al and its tetra-coordinated Al neighbor (**Figure 5b**). This structure is 0.311 eV more stable than the next most stable grafting site, due to the undercoordinated nature of the tri-coordinated Al in our model system (which may not be undercoordinated under operating conditions).[61] The most favorable location of the potassium promoter was probed by sampling 10

locations. A hydroxyl group was then added to the Fe site, to form K[($Al_sO)_2$Fe-OH], corresponding to species **B** in **Scheme 2**.

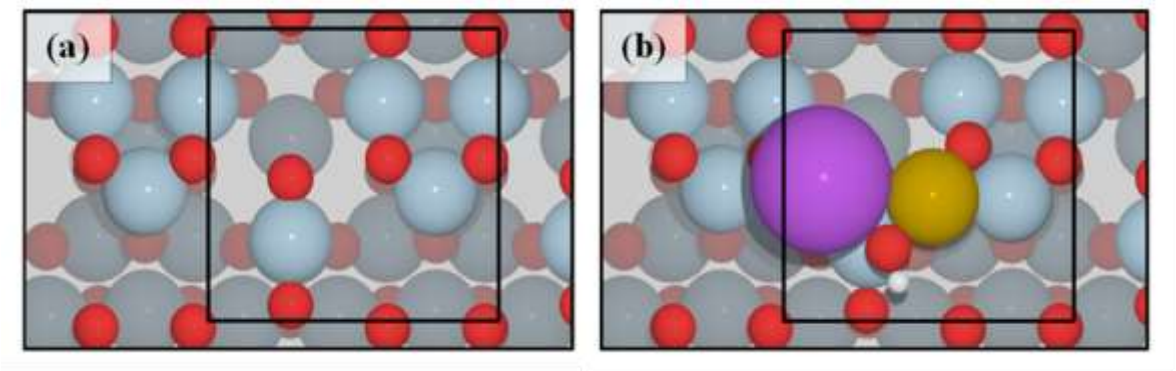


**Figure 5. (a)** Depiction of the (110) facet of fully dehydroxylated γ-$Al_2O_3$. The unit cell surface (black box) consists of three tetra-coordinated aluminum atoms and one tri-coordinated aluminum atom. Deeper layers are blurred for clarity. **(b)** Geometry of the model K[($Al_sO)_2$FeOH] active site. Color legend: Fe = gold, K = purple, surface Al/O = blue/red, subsurface Al/O = dark blue/light red, H = white.

Two $CO_2$ hydrogenation mechanisms were explored computationally. The first involves the formation of a hydroxycarbonyl intermediate, while the second involves formate formation. The mechanism involving the hydroxycarbonyl intermediate is shown in **Scheme 3**, which is fully analogous to **Scheme 2**. It is predicted to be faster than the formate mechanism based on the computed activation energies in the free energy diagrams (**Figure S18**). The calculations show that $H_2$ activation occurs by addition across the Fe-O bond, followed by proton migration to the hydroxyl ligand.

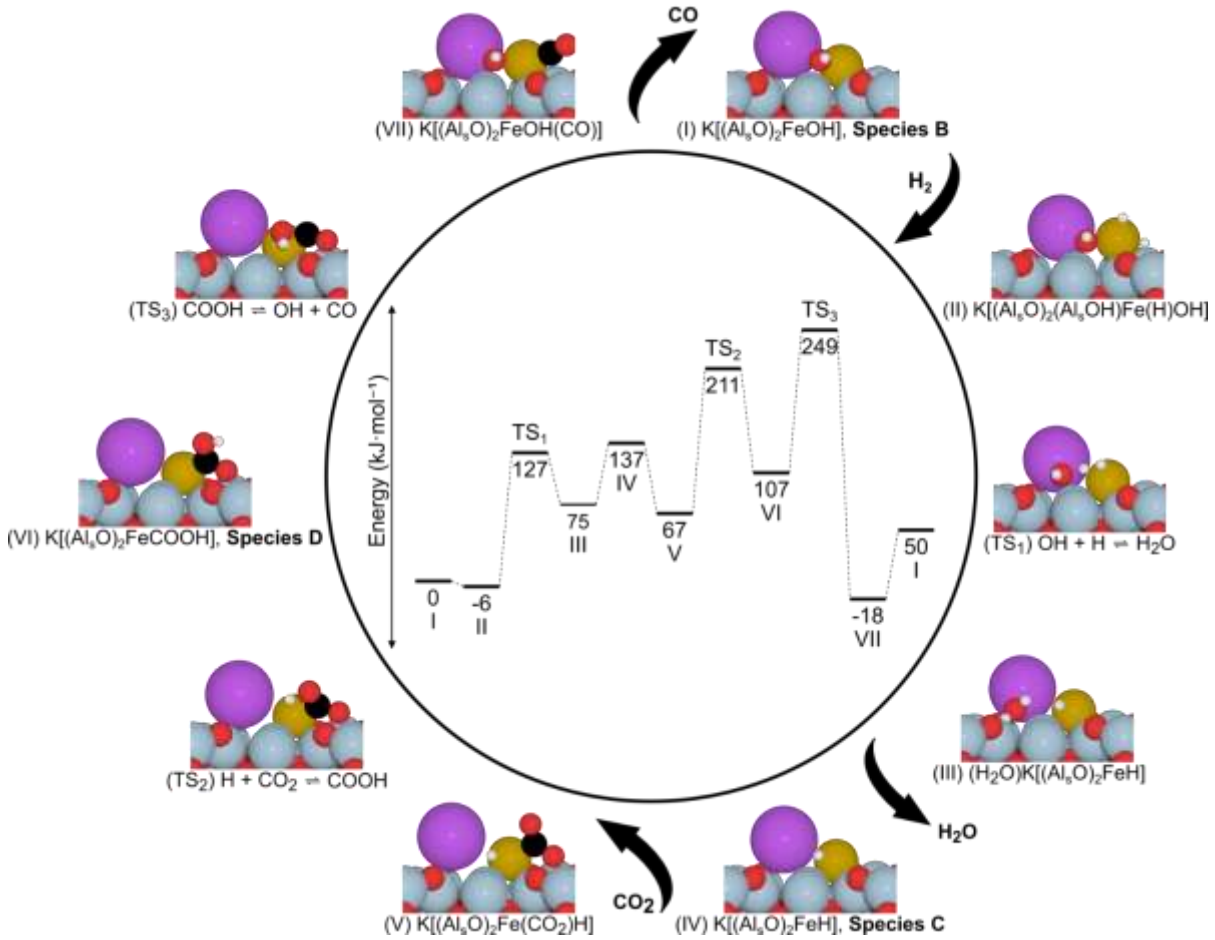


**Scheme 3.** Computed free energy diagram for the RWGS reaction, starting from the H[(Al$_s$O)$_2$FeOH] active site (**Species B**) derived from **2-K**. Computed at 400 °C and 30 bar ($CO_2/H_2$ = 1/3). Optimized geometries are shown for each state. Color scheme: Fe = gold, K = purple, Al = blue, O = pink/red, H = white, C = black. The energy difference between the start and end of the cycle (species **B**, state I) corresponds to the combined energies of the gas phase species.

**Table 3.** Computed free energies ($\Delta G$) and selected activation barriers ($\Delta G^{\ddagger}$) at 400 °C and 30 bar for steps in the RWGS mechanism shown in Scheme 3.

| Step | Mechanistic step | Free Energy (kJ/mol)[a] | |
|---|---|---|---|
| | | $\Delta G$ | $\Delta G^{\ddagger}$ |
| I-II | K[(Al$_s$O)$_2$FeOH] **(B)** + $H_{2(g)}$ → K[(Al$_s$O)(Al$_s$OH)Fe(H)OH] | -5.6 | - |
| II-III | K[(Al$_s$O)(Al$_s$OH)Fe(H)OH] → ($H_2$O)K[(Al$_s$O)$_2$FeH] | 81.0 | 132.9 |
| III-IV | ($H_2$O)K[(Al$_s$O)$_2$FeH] → K[(Al$_s$O)$_2$FeH] **(C)** + $H_2O_{(g)}$ | 61.4 | - |
| IV-V | K[(Al$_s$O)$_2$FeH] **(C)** + $CO_{2(g)}$ → K[(Al$_s$O)$_2$Fe($CO_2$)H] | -69.9 | - |
| V-VI | K[(Al$_s$O)$_2$Fe($CO_2$)H] → K[(Al$_s$O)$_2$FeCOOH] **(D)** | 40.3 | 143.7 |
| VI-VII | K[(Al$_s$O)$_2$FeCOOH) **(D)** → K[(Al$_s$O)$_2$Fe(CO)OH] | -125.2 | 141.5 |
| VII-I | K[(Al$_s$O)$_2$Fe(CO)OH] → K[(Al$_s$O)$_2$FeOH] **(B)** + $CO_{(g)}$ | 68.2 | - |

[a] All energies are reported relative to K[(Al$_s$O)$_2$FeOH] (state I) + $CO_{2(g)}$ + $H_{2(g)}$.

A mean–field microkinetic model was used to investigate the RWGS kinetics at temperatures from 250 to 550 °C and 30 bar total pressure. The free energies of reaction and activation free energies at 400 °C and 30 bar are shown in **Table 3**. $H_2O$ formation in $(H_2O)K[(Al_sO)_2FeH]$ (Step II-III) and the deinsertion of CO from $K[(Al_sO)_2FeCOOH)$ **D** to give $K[(Al_sO)_2FeOH(CO)]$ (Step VI-VII) are predicted to be the elementary steps with the greatest degree of rate control at temperatures below 200 °C. However, at higher temperatures, CO deinsertion from iron hydroxycarbonyl **D** (Step VI-VII) is predicted to control the overall rate of reaction (**Figure S19**).

The effect of temperature on the apparent activation barrier (**Figure S20**) and species coverage was also modeled. At 350 °C and 30 bar, the calculated apparent activation free energy is 302 kJ/mol due to the slow kinetics of hydroxycarbonyl formation and CO deinsertion. Surface coverage calculations indicate a transition in the dominant surface intermediate from $K[(Al_sO)_2FeOH]$ (**B**) to $K[(Al_sO)_2FeH]$ (**C**) as the temperature increases 350 to 400 °C at 30 bar (**Figure S21**). Below 350 °C, the rate law is predicted to be first-order with respect to $CO_2$ and half-order with respect to $H_2$ (**Figure S22**), which differs from the overall order obtained from experiment (2.0) in this temperature range. The predicted half-order for $H_2$ arises because of the predicted $H_2$ dissociative adsorption on species **B**. A mechanism that instead involves $H_2$ adsorption on **B** instead of dissociative adsorption would reconcile this difference in reaction orders—different FeK sites on different facets or phases of the alumina support may allow for this mechanism. Ultimately, further modeling and experiments will be necessary to understand how the phase and surface termination of alumina affect the RWGS microkinetics for this FeK catalyst and the structures of the postulated surface intermediates, as well as to clarify the role of the alkali metal promoters on catalyst stability, activity, and selectivity.

## Conclusions

Heterobimetallic iron complexes containing alkali metal cations ($M^+ = Li^+$, $K^+$, and $Na^+$), all with a molar ratio Fe:M = 1, were synthesized and grafted onto $Al_2O_3$ partially dehydroxylated at 500 °C. In the case of $[\{(THF)_2KFe(O\textit{t}Bu)_3\}_2]$, the iron surface complex was characterized by ICP, IR, XPS, EDX, XAFS, and EPR. XAFS spectroscopy revealed the grafted iron site to be an anionic Fe(II) complex coordinated by two *tert*-butoxide ligands and one anionic surface oxygen, associated with $K^+$. This material is active in the reverse water-gas shift reaction, with essentially 100% selectivity to CO at 400 °C. The $Na^+$ and $Li^+$ analogs both showed lower activity and reduced CO selectivity compared to the $K^+$ analog. All alkali metals should promote $CO_2$ adsorption, but $K^+$ appears to enhance the stability of the isolated Fe(II) sites, preventing their aggregation. The postulated mechanism proceeds through $H_2$ activation on an $K[(Al_sO)_2FeOH]$ site to form an iron hydride, which evolves to an iron hydroxycarbonyl intermediate $K[(Al_sO)_2FeCOOH]$ upon insertion of $CO_2$. Using earth-abundant single-site catalysts with tailored alkali metal promoters is a promising strategy to tune the activity, selectivity and stability for RWGS and other environmentally beneficial reactions.

## Conflicts of interest

There are no conflicts to declare.

## Data availability

Information and data on the synthesis of molecular complexes and catalyst preparation and characterization as well as computational modeling procedures are in the SI.

## Supporting Information

Details of DFT and microkinetic modeling and microkinetic simulation results, as well as structural characterization and kinetic data for catalysts.

**Acknowledgements**

A.A.I. thanks the Petroleum Technology Development Fund (PTDF) and Usmanu Danfodiyo University Sokoto, Nigeria, for a scholarship and study leave. L.L. and S.L.S. acknowledge support by the U.S. Department of Energy, Office of Science, Division of Basic Energy Sciences, under the Catalysis Science Initiative (DE-FG-02-03ER15467). Use of the Stanford Synchrotron Radiation Light source, SLAC National Accelerator Laboratory, is supported by the U.S. Department of Energy, Office of Science, Office of Basic Energy Sciences, under Contract DE-AC02-76SF00515.

**Corresponding Author Emails**

**Susannah L. Scott**: sscott@ucsb.edu

**Bryan R. Goldsmith**: bgoldsm@umich.edu

**Mostafa Taoufik**: mostafa.taoufik@univ-lyon1.fr

**References**

(1) Mac Dowell, N.; Fennell, P. S.; Shah, N.; Maitland, G. C. The Role of CO2 Capture and Utilization in Mitigating Climate Change. *Nat. Clim. Change* **2017**, *7* (4), 243–249. https://doi.org/10.1038/NCLIMATE3231.

(2) Wang, Z.; Song, H.; Liu, H.; Ye, J. Coupling of Solar Energy and Thermal Energy for Carbon Dioxide Reduction: Status and Prospects. *Angew. Chem.-Int. Ed.* **2020**, *59* (21), 8016–8035. https://doi.org/10.1002/anie.201907443.

(3) Cuellar-Franca, R. M.; Azapagic, A. Carbon Capture, Storage and Utilisation Technologies: A Critical Analysis and Comparison of Their Life Cycle Environmental Impacts. *J. CO2 Util.* **2015**, *9*, 82–102. https://doi.org/10.1016/j.jcou.2014.12.001.

(4) Jiang, Z.; Xiao, T.; Kuznetsov, V. L.; Edwards, P. P. Turning Carbon Dioxide into Fuel. *Philos. Trans. R. Soc. -Math. Phys. Eng. Sci.* **2010**, *368* (1923), 3343–3364. https://doi.org/10.1098/rsta.2010.0119.

(5) Daza, Y. A.; Kuhn, J. N. CO2 Conversion by Reverse Water Gas Shift Catalysis: Comparison of Catalysts, Mechanisms and Their Consequences for CO2 Conversion to Liquid Fuels. *RSC Adv.* **2016**, *6* (55), 49675–49691. https://doi.org/10.1039/c6ra05414e.

(6) Ali, N.; Bilal, M.; Nazir, M. S.; Khan, A.; Ali, F.; Iqbal, H. M. N. Thermochemical and Electrochemical Aspects of Carbon Dioxide Methanation: A Sustainable Approach to Generate Fuel via Waste to Energy Theme. *Sci. Total Environ.* **2020**, *712*, 136482. https://doi.org/10.1016/j.scitotenv.2019.136482.

(7) Galadima, A.; Muraza, O. Catalytic Thermal Conversion of CO2 into Fuels: Perspective and Challenges. *Renew. Sustain. Energy Rev.* **2019**, *115*, 109333. https://doi.org/10.1016/j.rser.2019.109333.

(8) Garba, M. D.; Usman, M.; Khan, S.; Shehzad, F.; Galadima, A.; Ehsan, M. F.; Ghanem, A. S.; Humayun, M. CO2 towards Fuels: A Review of Catalytic Conversion of Carbon Dioxide to Hydrocarbons. *J. Environ. Chem. Eng.* **2021**, *9* (2), 104756. https://doi.org/10.1016/j.jece.2020.104756.
(9) Olajire, A. A. Valorization of Greenhouse Carbon Dioxide Emissions into Value-Added Products by Catalytic Processes. *J. CO2 Util.* **2013**, *3–4*, 74–92. https://doi.org/10.1016/j.jcou.2013.10.004.
(10) Grignard, B.; Gennen, S.; Jerome, C.; Kleij, A. W.; Detrembleur, C. Advances in the Use of CO2 as a Renewable Feedstock for the Synthesis of Polymers. *Chem. Soc. Rev.* **2019**, *48* (16), 4466–4514. https://doi.org/10.1039/c9cs00047j.
(11) Huang, J.; Buonsanti, R. Colloidal Nanocrystals as Heterogeneous Catalysts for Electrochemical CO2 Conversions. *Chem. Mater.* **2019**, *31* (1), 13–25. https://doi.org/10.1021/acs.chemmater.8b04155.
(12) Xu, L.; Xiu, Y.; Liu, F.; Liang, Y.; Wang, S. Research Progress in Conversion of CO(2)to Valuable Fuels. *Molecules* **2020**, *25* (16), 3653. https://doi.org/10.3390/molecules25163653.
(13) Das, S.; Perez-Ramirez, J.; Gong, J.; Dewangan, N.; Hidajat, K.; Gates, B. C.; Kawi, S. Core-Shell Structured Catalysts for Thermocatalytic, Photocatalytic, and Electrocatalytic Conversion of CO2. *Chem. Soc. Rev.* **2020**, *49* (10), 2937–3004. https://doi.org/10.1039/c9cs00713j.
(14) Kaiser, P.; Unde, R. B.; Kern, C.; Jess, A. Production of Liquid Hydrocarbons with CO2 as Carbon Source Based on Reverse Water-Gas Shift and Fischer-Tropsch Synthesis. *Chem. Ing. Tech.* **2013**, *85* (4, SI), 489–499. https://doi.org/10.1002/cite.201200179.
(15) Zhuang, Y.; Currie, R.; McAuley, K. B.; Simakov, D. S. A. Highly-Selective CO2 Conversion via Reverse Water Gas Shift Reaction over the 0.5wt% Ru-Promoted Cu/ZnO/Al2O3 Catalyst. *Appl. Catal. A -Gen.* **2019**, *575*, 74–86. https://doi.org/10.1016/j.apcata.2019.02.016.
(16) He, Y.; Yang, K. R.; Yu, Z.; Fishman, Z. S.; Achola, L. A.; Tobin, Z. M.; Heinlein, J. A.; Hu, S.; Suib, S. L.; Batista, V. S.; Pfefferle, L. D. Catalytic Manganese Oxide Nanostructures for the Reverse Water Gas Shift Reaction. *NANOSCALE* **2019**, *11* (35), 16677–16688. https://doi.org/10.1039/c9nr06078b.
(17) Xu, X.; Moulijn, J. Mitigation of CO2 by Chemical Conversion: Plausible Chemical Reactions and Promising Products. *Energy Fuels* **1996**, *10* (2), 305–325.
(18) Xu, J.; Su, X.; Duan, H.; Hou, B.; Lin, Q.; Liu, X.; Pan, X.; Pei, G.; Geng, H.; Huang, Y.; Zhang, T. Influence of Pretreatment Temperature on Catalytic Performance of Rutile TiO2-Supported Ruthenium Catalyst in CO2 Methanation. *J. Catal.* **2016**, *333*, 227–237. https://doi.org/10.1016/j.jcat.2015.10.025.
(19) Nityashree, N.; Price, C. A. H.; Pastor-Perez, L.; Manohara, G. V.; Garcia, S.; Maroto-Valer, M. M.; Reina, T. R. Carbon Stabilised Saponite Supported Transition Metal-Alloy Catalysts for Chemical CO2 Utilisation via Reverse Water-Gas Shift Reaction. *Appl. Catal. B-Environ.* **2020**, *261*, 118241. https://doi.org/10.1016/j.apcatb.2019.118241.
(20) Su, X.; Yang, X.; Zhao, B.; Huang, Y. Designing of Highly Selective and High-Temperature Endurable RWGS Heterogeneous Catalysts: Recent Advances and the Future Directions. *J. Energy Chem.* **2017**, *26* (5), 854–867. https://doi.org/10.1016/j.jechem.2017.07.006.
(21) Chen, X.; Chen, Y.; Song, C.; Ji, P.; Wang, N.; Wang, W.; Cui, L. Recent Advances in Supported Metal Catalysts and Oxide Catalysts for the Reverse Water-Gas Shift Reaction. *Front. Chem.* **2020**, *8*, 709. https://doi.org/10.3389/fchem.2020.00709.
(22) Dou, J.; Sheng, Y.; Choong, C.; Chen, L.; Zeng, H. C. Silica Nanowires Encapsulated Ru Nanoparticles as Stable Nanocatalysts for Selective Hydrogenation of CO2 to CO. *Appl. Catal. B-Environ.* **2017**, *219*, 580–591. https://doi.org/10.1016/j.apcatb.2017.07.083.
(23) Panagiotopoulou, P. Hydrogenation of CO2 over Supported Noble Metal Catalysts. *Appl. Catal. A -Gen.* **2017**, *542*, 63–70. https://doi.org/10.1016/j.apcata.2017.05.026.
(24) Park, J.-N.; McFarland, E. W. A Highly Dispersed Pd-Mg/SiO2 Catalyst Active for Methanation of CO2. *J. Catal.* **2009**, *266* (1), 92–97. https://doi.org/10.1016/j.jcat.2009.05.018.

(25) Kwak, J. H.; Kovarik, L.; Szanyi, J. CO2 Reduction on Supported Ru/Al2O3 Catalysts: Cluster Size Dependence of Product Selectivity. *ACS Catal.* **2013**, *3* (11), 2449–2455. https://doi.org/10.1021/cs400381f.
(26) Matsubu, J. C.; Yang, V. N.; Christopher, P. Isolated Metal Active Site Concentration and Stability Control Catalytic CO2 Reduction Selectivity. *J. Am. Chem. Soc.* **2015**, *137* (8), 3076–3084. https://doi.org/10.1021/ja5128133.
(27) Doherty, F.; Goldsmith, B. R. Rhodium Single-Atom Catalysts on Titania for Reverse Water Gas Shift Reaction Explored by First Principles Mechanistic Analysis and Compared to Nanoclusters. *ChemCatChem* **2021**, *13* (13), 3155–3164. https://doi.org/10.1002/cctc.202100292.
(28) Doherty, F.; Wang, H.; Yang, M.; Goldsmith, B. R. Nanocluster and Single-Atom Catalysts for Thermocatalytic Conversion of CO and CO2. *Catal. Sci. Technol.* **2020**, *10* (17), 5772–5791. https://doi.org/10.1039/d0cy01316a.
(29) Zhu, X.; Shen, M.; Lobban, L. L.; Mallinson, R. G. Structural Effects of Na Promotion for High Water Gas Shift Activity on Pt-Na/TiO2. *J. Catal.* **2011**, *278* (1), 123–132. https://doi.org/10.1016/j.jcat.2010.11.023.
(30) Yang, M.; Li, S.; Wang, Y.; Herron, J. A.; Xu, Y.; Allard, L. F.; Lee, S.; Huang, J.; Mavrikakis, M.; Flytzani-Stephanopoulos, M. Catalytically Active Au-O(OH)(x)-Species Stabilized by Alkali Ions on Zeolites and Mesoporous Oxides. *Science* **2014**, *346* (6216), 1498–1501. https://doi.org/10.1126/science.1260526.
(31) Bando, K.; Soga, K.; Kunimori, K.; Arakawa, H. Effect of Li Additive on CO2 Hydrogenation Reactivity of Zeolite Supported Rh Catalysts. *Appl. Catal. A -Gen.* **1998**, *175* (1–2), 67–81.
(32) Goguet, A.; Meunier, F.; Tibiletti, D.; Breen, J.; Burch, R. Spectrokinetic Investigation of Reverse Water-Gas-Shift Reaction Intermediates over a Pt/CeO2 Catalyst. *J. Phys. Chem. B* **2004**, *108* (52), 20240–20246. https://doi.org/10.1021/jp047242w.
(33) Loiland, J. A.; Wulfers, M. J.; Marinkovic, N. S.; Lobo, R. F. Fe/Gamma-Al2O3 and Fe-K/Gamma-Al2O3 as Reverse Water-Gas Shift Catalysts. *Catal. Sci. Technol.* **2016**, *6* (14), 5267–5279. https://doi.org/10.1039/c5cy02111a.
(34) Choi, P. H.; Jun, K. W.; Lee, S. J.; Choi, M. J.; Lee, K. W. Hydrogenation of Carbon Dioxide over Alumina Supported Fe-K Catalysts. *Catal. Lett.* **1996**, *40* (1–2), 115–118. https://doi.org/10.1007/BF00807467.
(35) Yang, X.; Su, X.; Chen, X. D.; Duan, H. M.; Liang, B. L.; Liu, Q. G.; Liu, X. Y.; Ren, Y. J.; Huang, Y., Q.; Zhang, T. Promotion Effects of Potassium on the Activity and Selectivity of Pt/Zeolite Catalysts for Reverse Water Gas Shift Reaction. *Appl. Catal. B-Environ.* **2017**, *216*, 95–105. https://doi.org/10.1016/j.apcatb.2017.05.067.
(36) Bonetto, R.; Crisanti, F.; Sartorel, A. Carbon Dioxide Reduction Mediated by Iron Catalysts: Mechanism and Intermediates That Guide Selectivity. *ACS Omega* **2020**, *5* (34), 21309–21319. https://doi.org/10.1021/acsomega.0c02786.
(37) Franken, T.; Heel, A. Are Fe Based Catalysts an Upcoming Alternative to Ni in CO2 Methanation at Elevated Pressure? *J. CO2 Util.* **2020**, *39*, 101175. https://doi.org/10.1016/j.jcou.2020.101175.
(38) Samantaray, M. K.; D'Eia, V.; Pump, E.; Falivene, L.; Harb, M.; Chikh, S. O.; Cavallo, L.; Basset, J.-M. The Comparison between Single Atom Catalysis and Surface Organometallic Catalysis. *Chem. Rev.* **2020**, *120* (2), 734–813. https://doi.org/10.1021/acs.chemrev.9b00238.
(39) Le Quemener, F.; Barman, S.; Merle, N.; Aljuhani, M. A.; Samantaray, M. K.; Saih, Y.; Szeto, K. C.; De Mallmann, A.; Minenkov, Y.; Huang, K.-W.; Cavallo, L.; Taoufik, M.; Basset, J.-M. Metathetic Oxidation of 2-Butenes to Acetaldehyde by Molecular Oxygen Using the Single-Site Olefin Metathesis Catalyst ( SiO)(2)Mo(=O)(2). *ACS Catal.* **2018**, *8* (8), 7549–7555. https://doi.org/10.1021/acscatal.8b01767.
(40) Gun'ko, Y.; Cristmann, U.; Kessler, V. Synthesis and Structure of the First Fe-II Heterometallic Alkoxide [(THF)NaFe(OtBu)(3)](2) - a Possible Precursor for New Materials. *Eur. J. Inorg. Chem.* **2002**, 5, 1029–1031.

(41) Chambers, M. B.; Groysman, S.; Villagran, D.; Nocera, D. G. Iron in a Trigonal Tris(Alkoxide) Ligand Environment. *Inorg. Chem.* **2013**, *52* (6), 3159–3169. https://doi.org/10.1021/ic302634q.
(42) Delgado, M.; Delbecq, F.; Santini, C. C.; Lefebvre, F.; Norsic, S.; Putaj, P.; Sautet, P.; Basset, J.-M. Evolution of Structure and of Grafting Properties of γ-Alumina with Pretreatment Temperature. *J. Phys. Chem. C* **2012**, *116* (1), 834–843. https://doi.org/10.1021/jp208709x.
(43) Kresse, G.; Hafner, J. Norm-Conserving and Ultrasoft Pseudopotentials for First-Row and Transition-Elements. *J. Phys.-Condens. Matter* **1994**, *6* (40), 8245–8257. https://doi.org/10.1088/0953-8984/6/40/015.
(44) Kresse, G.; Furthmuller, J. Efficient Iterative Schemes for Ab Initio Total-Energy Calculations Using a Plane-Wave Basis Set. *Phys. Rev. B* **1996**, *54* (16), 11169–11186. https://doi.org/10.1103/PhysRevB.54.11169.
(45) Kresse, H.; Rabenstein, P. Geometrical Aspects and Dipole-Dipole Interaction in a Liquid-Crystalline Mixture. *Phys. Stat. Sol. (a)* **1987**, *100* (1), K83–K85. https://doi.org/10.1002/pssa.2211000163.
(46) Grimme, S.; Antony, J.; Ehrlich, S.; Krieg, H. A Consistent and Accurate Ab Initio Parametrization of Density Functional Dispersion Correction (DFT-D) for the 94 Elements H-Pu. *J. Chem. Phys.* **2010**, *132* (15), 154104. https://doi.org/10.1063/1.3382344.
(47) Gu, J.; Wang, J.; Leszczynski, J. Single Fe Site on the Surface of Gamma-Al2O3: Insights from Density Functional Theory Periodic Boundary Approach. *J. Phys. Chem. C* **2020**, *124* (38), 20931–20941. https://doi.org/10.1021/acs.jpcc.0c05401.
(48) Wischert, R.; Laurent, P.; Coperet, C.; Delbecq, F.; Sautet, P. Gamma-Alumina: The Essential and Unexpected Role of Water for the Structure, Stability, and Reactivity of "Defect" Sites. *J. Am. Chem. Soc.* **2012**, *134* (35), 14430–14449. https://doi.org/10.1021/ja3042383.
(49) Cholewins, M. C.; Dixit, M.; Mpourmpakis, G. Computational Study of Methane Activation on Gamma-Al2O3. *ACS Omega* **2018**, *3* (12), 18242–18250. https://doi.org/10.1021/acsomega.8b02554.
(50) Larabi, C.; Norsic, S.; Khrouz, L.; Boyron, O.; Szeto, K. C.; Lucas, C.; Taoufik, M.; De Mallmann, A. Oxide-Supported Titanium Catalysts: Structure-Activity Relationship in Heterogeneous Catalysis, with the Choice of Support as a Key Step. *Organometallics* **2020**, *39* (24), 4608–4617. https://doi.org/10.1021/acs.organomet.0c00650.
(51) Wagner, C. Sensitity Factors for XPS Analysis of Surface Atoms. *J. Electron Spectrosc. Relat. Phenom.* **1983**, *32* (2), 99–102. https://doi.org/10.1016/0368-2048(83)85087-7.
(52) Kuivila, C.; Butt, J.; Stair, P. Characterization of Surface Species on Iron Synthesis Catalysts by X-Ray Photoelectron-Spectroscopy. *Appl. Surf. Sci.* **1988**, *32* (1–2), 99–121. https://doi.org/10.1016/0169-4332(88)90076-1.
(53) Siriwardane, R.; Poston, J. Characterization of Copper Oxides, Iron-Oxides, and Zinc Copper Ferrite Desulfurzation Sorbents by X-Ray Photoelectron-Spectroscopy and Scanning Electron-Microscopy. *Appl. Surf. Sci.* **1993**, *68* (1), 65–80. https://doi.org/10.1016/0169-4332(93)90216-X.
(54) Brant, P.; Feltham, R. X-Ray Photoelectron-Spectra of Iron Complexes - Correlation of Iron-2P Satellite Intensity with Complex Spin State. *J. Electron Spectrosc. Relat. Phenom.* **1983**, *32* (3), 205–221. https://doi.org/10.1016/0368-2048(83)85002-6.
(55) Smith, M. Monomer-Dimer Equilibria of Liquid Aluminum Alkyls.2. Triisobutylaluminum. *J. Organomet. Chem.* **1970**, *22* (2), 273–281. https://doi.org/10.1016/S0022-328X(00)86043-X.
(56) Mazoyer, E.; Trebosc, J.; Baudouin, A.; Boyron, O.; Pelletier, J.; Basset, J.-M.; Vitorino, M. J.; Nicholas, C. P.; Gauvin, R. M.; Taoufik, M.; Delevoye, L. Heteronuclear NMR Correlations To Probe the Local Structure of Catalytically Active Surface Aluminum Hydride Species on Gamma-Alumina. *Angew. Chem.-Int. Ed.* **2010**, *49* (51), 9854–9858. https://doi.org/10.1002/anie.201004310.
(57) Iffland, L.; Khedkar, A.; Petuker, A.; Lieb, M.; Wittkamp, F.; van Gastel, M.; Roemelt, M.; Apfel, U.-P. Solvent-Controlled CO2 Reduction by a Triphos-Iron Hydride Complex. *Organometallics* **2019**, *38* (2), 289–299. https://doi.org/10.1021/acs.organomet.8b00711.

(58) Liu, Y.-Z.; Li, X.-N.; He, S.-G. Reactivity of Iron Hydride Anions Fe2Hn- (N=0-3) with Carbon Dioxide. *J. Phys. Chem. A* **2020**, *124* (41), 8414–8420. https://doi.org/10.1021/acs.jpca.0c06986.
(59) Habib, M.; Sarkar, R.; Biswas, S.; Pramanik, A.; Sarkar, P.; Pal, S. Unambiguous Hydrogenation of CO2 by Coinage-Metal Hydride Anions: An Intuitive Idea Based on in Silico Experiments. *Phys. Chem. Chem. Phys.* **2019**, *21* (14), 7483–7490. https://doi.org/10.1039/c9cp00133f.
(60) Schneck, F.; Ahrens, J.; Finger, M.; Stueckl, A. C.; Wuertele, C.; Schwarzer, D.; Schneider, S. The Elusive Abnormal CO2 Insertion Enabled by Metal-Ligand Cooperative Photochemical Selectivity Inversion. *Nat. Commun.* **2018**, *9*, 1161. https://doi.org/10.1038/s41467-018-03239-3.
(61) Zhang, F.; Szeto, K. C.; Taoufik, M.; Delevoye, L.; Gauvin, R. M.; Scott, S. L. Enhanced Metathesis Activity and Stability of Methyltrioxorhenium on a Mostly Amorphous Alumina: Role of the Local Grafting Environment. *J. Am. Chem. Soc.* **2018**, *140* (42), 13854–13868. https://doi.org/10.1021/jacs.8b08630.